X-ray photoelectron spectroscopy (XPS) and radiation shielding parameters investigations for zinc molybdenum borotellurite glasses containing different network modifiers

G. Lakshminarayana[1,*] , S. O. Baki[2], A. Lira[3], M. I. Sayyed[4], I. V. Kityk[5,6], M. K. Halimah[2], and M. A. Mahdi[1]

[1] *Wireless and Photonic Networks Research Centre, Faculty of Engineering, Universiti Putra Malaysia, 43400, Serdang, Selangor, Malaysia*

[2] *Department of Physics, Faculty of Science, Universiti Putra Malaysia, 43400 Serdang, Selangor, Malaysia*

[3] *Department of Physics, Faculty of Science, Autonomous University of Mexico State, 50000 Toluca, Mexico*

[4] *Department of Physics, Faculty of Science, University of Tabuk, Tabuk, Saudi Arabia*

[5] *Faculty of Electrical Engineering, Czestochowa University of Technology, Armii Krajowej 17, 42-217 Czestochowa, Poland*

[6] *Institute of Physics, University of Zielona Góra, Licealna 9, 65-407 Zielona Góra, Poland*

ABSTRACT

Zinc molybdenum borotellurite glasses containing different network modifiers with the nominal composition of 60 TeO_2–10 B_2O_3–10 MoO_3–10 ZnO–10 MO (MO = Li_2O, Na_2O, K_2O, MgO, CaO, and PbO) were prepared by melt quenching method. The X-ray photoelectron spectroscopy (XPS) studies allow to monitor the structural modifications leading to the formation of bridging oxygens (Te–O–Te, B–O–B, Mo–O–Mo, and Te–O–Mo bonds) and nonbridging oxygens (Te = O, Te–O^-M^+, Mo–O^- bonds in the MoO_6 octahedral units, Zn–O bonds from ZnO_4) with the addition of alkali (Li, Na, and K), alkaline (Mg, Ca), or heavy metal (Pb) oxides. The Te 3d localized core-levels spectra show an asymmetry due to the existence of different Te-based structural clusters and were fitted with three contributions such as Te ions in TeO_4 trigonal bipyramid configuration, Te ions in TeO_3^- trigonal pyramid configuration and TeO_{3+1} polyhedra, respectively. The analysis of the Mo 3d spectra indicates prevailingly Mo^{6+} ions only. The Zn 2p core-level XPS spectra demonstrate that the zinc is mainly coordinated by four oxygen atoms. The essential radiation shielding parameters were studied for the prepared glasses in the photon energy range 1 keV to 100 GeV using WinXCom software program. Parameters like mass attenuation coefficient (μ/ρ), effective atomic number (Z_{eff}), and mean free path

Address correspondence to E-mail: glnphysics@gmail.com

(MFP) are evaluated. Further, by using geometric progression method, exposure buildup factor (EBF) values were also calculated in the incident photon energy range 0.015–15 MeV, up to penetration depth of 40 mfp (mean free path). The macroscopic effective removal cross sections ($\sum_R$) for fast neutrons have been calculated. The maximum values of μ/ρ and Z_{eff} were found for PbO-introduced glass though it possesses a lower value for MFP and EBF. The obtained results indicate that PbO-based glass is the best radiation shielding material among the studied glasses.

Introduction

In the optical materials (e.g., glasses) research, it is well known that the optical properties and quantum efficiency of the rare-earth (RE) ions depend substantially on the ligand field environment around the RE ions site and phonon energy of the host glass matrix [1, 2]. Thus, it is crucial to find a suitable host glass matrix for RE ions doping due to their important role in the fabrication of efficient lasers, optical amplifiers, and optoelectronic devices. Recently, one can find an enhanced interest among researchers for the addition of two or more glass formers to fabricate host glass for the RE ions doping with attractive optical properties for their potential scientific and technological applications [3–7]. So, it becomes necessary to design a particular composition of glasses keeping in view of the requirement and optimize them for the production of highly significant and useful optical devices.

It is well known that among several glass formers (SiO_2, P_2O_5, GeO_2, As_2O_3, etc.,), boric acid (B_2O_3) is one of the excellent glass formers and can form glass with high thermal stability, better chemical durability, good optical transparency, and considered promising candidate for RE ions doping [8–11]. Usually, the doped RE ions retain most of their individual properties in the glass matrix. However, borate glasses possess relatively higher phonon energy (~ 1300–1500 cm^{-1}), which leads to nonradiative transitions in RE ions and restricts their use in practical applications. On the other hand, tellurite-rich glasses exhibit good mechanical stability, chemical durability, low melting point, low phonon energy (~ 700–800 cm^{-1}), high linear and nonlinear refractive indices, high RE ion solubility (10–50 times larger than in silica) without inducing crystallization, and a wide optical transparency window (typically 0.4–6 μm), which make them promising materials for

photonic applications such as lasers [12], optical fiber amplifiers [13, 14], nonlinear optical devices [15], and planar waveguides [16]. These fascinating properties of tellurite-rich glasses are mainly caused by the high polarizability of the Te^{4+}-ions (1.595 Å), which possess a nonbonding electron lone pair 5s^{2}5p^0. In fact, tellurium dioxide (TeO_2) is a conditional glass former and does not have the ability to form glass itself under normal quenching rates/conditions and TeO_2 requires addition of modifiers such as alkali or alkaline earth and transition metal oxides or other glass formers, for example, B_2O_3 to form glass [17–19].

Based on the above description of borate and tellurite glasses, one can expect that borotellurite glasses should demonstrate a suitable compromise between the requirements of low phonon energy, wide transparency in near- and far-infrared regions, relatively high thermal stability, good chemical durability, and ease of glass fabrication [20, 21]. All these parameters are crucial for the fabrication of optical fibers. It is well known that addition of zinc oxide (ZnO) to borotellurite glass network produces low rates of crystallization and increases the glass-forming ability (GFA) [22–24].

In TeO_2-based glasses, MoO_3 improves the functionality of glasses; as an example, Chung et al. [25] recently reported that the addition of MoO_3 into tellurite glasses shows ~ 1.5 times wider Raman scattering bandwidth, without any significant decrease in Raman gain coefficient than that of the tellurite glass without MoO_3. It was identified that the characteristic Mo = O bonds formed by MoO_3 addition in sodium–zinc–tellurite glass network are mainly responsible for the obtained flatter Raman scattering band [25]. In tellurite glasses, usually, the MoO_3 addition exhibits vibrational modes like Mo–O–Mo, and Mo = O in the Raman spectra with energy higher than 800 cm^{-1} [25–27], which considerably increases the phonon energy of the glasses. In optical glasses, structural

studies are of high importance owing to the interrelation between the medium-range atomic arrangement and properties. In glass formers, alkali or alkaline and heavy metal oxide modifiers such as Li, Na, K, Mg, Ca, and Pb usually enhance the GFA by altering or breaking chains of structural units causing changes or modifications in structural units and by increasing the entropy of the glass [17, 28]. Usually, the type and the amount of the modifier oxide in the glass composition will play a crucial role in the properties of the host glasses. It is well known that the addition of alkali and/or alkaline earth modifiers or heavy metal oxides to the tellurite-rich network causes a change of the Te-coordinated polyhedron (breakage of bridging oxygen (BO) bonds) from TeO_4 trigonal bipyramid (tbp) to TeO_{3+1}, then to TeO_3 trigonal pyramid (tp), in which one of the Te sp^3 hybrid orbitals is occupied by a lone pair of electrons [28–30]. This transformation also causes an increase in the number of nonbridging oxygen (NBO) atoms due to increasing molar mass from Li to K, Mg to Ba or Pb and also to accommodate themselves into the glass network matrix during the glass formation [17, 28].

In the field of radiation physics, optical glasses can be used as an alternative and effective shielding material to concrete or in combination with concrete. It is well known that the traditional radiation shielding material, concrete is opaque to the visible light and deterioration of mechanical properties occurs when it is exposed to the γ-radiations for longer periods of time. For this purpose, very recently, there has been an increasing interest among researchers in the evaluation of different kinds of optical glasses such as tellurite, phosphates, borates, and silicates as new radiation shielding materials for their possible applications in gamma radiation detection [31–35].

In our recent publication [28], we have reported a comprehensive analysis of the physical, structural, thermal, and optical spectroscopy properties of TeO_2–B_2O_3–MoO_3–ZnO–R_2O (R = Li, Na, and K)/ MO (M = Mg, Ca, and Pb) glasses. In the present work, we have performed the XPS measurements for alkali (Li-, Na-, K-), alkaline (Mg-, Ca-), and heavy metal (Pb) oxide-based zinc molybdenum borotellurite glasses in order to study their microstructural properties. We also report the essential radiation shielding parameters such as mass attenuation coefficient (μ/ρ), effective atomic number (Z_{eff}), and

mean free path (MFP) for these glasses. The macroscopic effective removal cross sections ($\sum_R$) for fast neutrons have also been evaluated.

Experimental

Synthesis

The synthesis of the studied glasses was described in detail in our recent publication [28]. In brief, the conventional melt quenching method was used to prepare the zinc molybdenum borotellurite glasses containing different network modifier ions such as Li, Na, K, Mg, Ca, and Pb. The starting materials used in the present work were high-purity TeO_2 (99.995%), B_2O_3 (99.98%), MoO_3 (99.97%), ZnO (99.99%), Li_2CO_3 (99.99%), Na_2CO_3 (99.5%), K_2CO_3 (≥99%), MgO (99.99%), anhydrous CaO (≥99.99%), and PbO (≥99). All the chemicals were purchased from Sigma–Aldrich. The nominal composition of the glasses synthesized in this work was 60 TeO_2–10 B_2O_3–10 MoO_3–10 ZnO–10 MO (MO = Li_2O, Na_2O, K_2O, MgO, CaO, and PbO). The synthesized six glasses are indicated as "G1" (Li_2O), "G2" (Na_2O), "G3" (K_2O), "G4" (MgO), "G5" (CaO), and "G6" (PbO), respectively, for convenience. All the appropriate chemicals were weighed in the stoichiometric ratio in 20-g batch each separately, thoroughly mixed using an agate mortar and a pestle, and then, each of those powders is collected into a high-purity alumina crucible and heated in an electric furnace for melting at 930 °C for 30 min. The melts were subsequently poured onto a stainless steel plate and then quickly pressed with another steel plate. The obtained glass disks were optically transparent, having a diameter of 3–4 cm and a thickness of ∼0.3 cm. The internal stress induced in the glasses during the melt quenching was released by annealing the samples below glass transition temperature at 300 °C for 5 h in air and then allowed to cool down slowly to ambient temperature. Finally, the glass samples were prepared in powder form for XPS measurements.

XPS characterization

The glass powders chemical composition, as well as the local chemical environments, was analyzed using Kratos Axis Ultra DLD XPS spectrometer in an ultrahigh vacuum chamber (base pressure ∼ 10^{-9} Torr).

The XPS data sets were collected with a monochromatic Mg K_α X-ray source at an output power of 150 watts with a photon energy of 1253.6 eV and a step size of ~1.0 eV and 0.1 eV, respectively, for the survey (wide) scan and high-resolution (narrow) spectra. Survey scans (~1.0-eV step size) were performed with the pass energy of 160 eV to gain qualitative information such as peak identification and peak position. Peaks identified in all the survey scans were used to adjust high-resolution scan binding energy range with pass energy, 20 eV. The analyzed area was equal to 300×700 μm in diameter. For self-consistency, the measured binding energy of the peaks was corrected based on the calibration factor calculated from the difference between the measured binding energy of the C 1s peak and its reference value of 284.6 eV. Here, the C 1s peak generally originates from hydrocarbon contamination and its binding energy (BE) is usually assumed to be constant, irrespective of the chemical oxidation state of the material.

Radiation shielding parameters: theoretical basis and method of computation

Mass attenuation coefficient

The mass attenuation coefficient (μ/ρ) is a measure of the average number of interactions for the gamma rays with a material that occur in a particular mass per unit area thickness of the material. When a narrow beam of monoenergetic photons penetrates a layer of material with thickness t, it follows the Lambert–Beer law given by [36]:

$$I = I_0 \exp^{[-(\mu/\rho)t]} \tag{1}$$

where I_0 and I are the incident and transmission intensity, respectively, t is the sample thickness, and μ/ρ is the mass attenuation coefficient (in $cm^2\ g^{-1}$).

For materials, which consist of different elements, it is assumed that the contribution of each element of the material to the total photon attenuation is additive. In such case, the μ/ρ can be calculated using the following relation [37]:

$$\mu/\rho = \sum_i w_i (\mu/\rho)_i \tag{2}$$

where w_i is the proportion by weight and $(\mu/\rho)_i$ is mass attenuation coefficient of the ith element, which can be calculated by using WinXCom software [38].

Effective atomic number

The values of μ/ρ are then utilized to evaluate the photon interaction cross section (σ_t) of the glasses though the following equation [39]:

$$\sigma_t = \frac{M(\mu/\rho)}{N_A} \tag{3}$$

where $M = \sum A_i n_i$, the molecular weight of the sample, A_i, is the atomic weight of the ith element, n_i is the number of formula units of a molecule, and N_A is the Avogadro's number.

Effective atomic cross section σ_a is calculated by using the following equation [40]:

$$\sigma_a = \frac{\sigma_t}{\sum_i n_i} \tag{4}$$

Total electronic cross section σ_e is calculated by [40]:

$$\sigma_e = \frac{1}{N_A} \sum_i \frac{f_i A_i}{Z_i} (\mu_m)_i \tag{5}$$

where f_i and Z_i represent the fractional abundance of the element "i" and the atomic number of the constituent element, respectively.

Finally, the following relation was used to calculate the effective atomic number (Z_{eff}) [40]

$$Z_{eff} = \frac{\sigma_a}{\sigma_e} \tag{6}$$

Mean free path

The mean free path (MFP) of any material is the term to depict the effectiveness of gamma-ray shielding. It can be defined as the average travelled distance between two successive photon interactions [41]. The lower MFP indicates more interaction of gamma rays with the material; hence, the better shielding properties can be obtained. The MFP is calculated using the relationship [42]:

$$MFP = \frac{1}{\mu} \tag{7}$$

where μ is the linear attenuation coefficient (mass attenuation coefficient value multiplied by the density of the sample).

Exposure buildup factor (EBF)

To calculate the EBF, the GP fitting parameters were obtained using logarithmic interpolation method

from the equivalent atomic number (Z_{eq}). Z_{eq} is a parameter, which describes the composite material properties in terms of equivalent elements similar to atomic number for a single element. The photoelectric absorption and pair production are both the photon removal processes. Therefore, the buildup of photons in a medium is mainly due to the multiple scattering events in Compton scattering region, so that Z_{eq} is derived from the Compton scattering interaction process. For the detailed knowledge on the calculations of the Z_{eq} and EBF of the glasses, the readers can refer to Refs [43–45].

Macroscopic effective removal cross section for fast neutrons ($\sum_R$)

The macroscopic effective removal cross section for fast neutrons is the probability of one neutron undergoing a particular reaction per unit path length of travel through the shielding medium. The following relation was used to evaluate the $\sum_R$ for the selected glass samples [46]:

$$\sum_R = \sum_i W_i \left(\sum_R / \rho \right)_i \tag{8}$$

where W_i is the partial density (g cm^{-3}) and $\sum_{R/\rho}$ (cm^2 g^{-1}) is the mass removal cross section of the ith constituent obtained from [47, 48].

Results and discussion

XPS analysis of G1–G6 glasses

A thorough analysis of structural, thermal, and optical absorption properties for Li-, Na-, K-, Mg-, Ca-, and Pb oxide-based glasses (labeled here as "G1," "G2," "G3," "G4," "G5," and "G6," respectively) was reported by us, recently in Ref. [28]. In this article, we analyze the XPS spectral data for deeper understanding of the local environment of the Te atoms and to obtain an information about the BOs and NBOs, TeO$_4$ and TeO$_3$/TeO$_{3+1}$ structural units, molybdenum (Mo), and zinc (Zn) oxidation states, which could present in the G1–G6 glasses network matrices.

It is well known that the XPS is an important experimental technique to evaluate the environment of particular atoms for a given matrix composition and the fusibility of various chemicals used during the glass synthesis and it provides chemical oxidation states and bonding information of atoms [49]. Generally, XPS of solids consists of core-levels and valence band and the intensity of core-levels decreases with decreasing BE where BE for a given level is assigned to a particular element. Particularly, within the solid, the BE of core electron is affected by both the local electron density around the atom and structural arrangement (chemical bonding) for the other atoms and this is generally defined as a chemical shift in the XPS spectra [50, 51].

Relatively low-resolution XPS survey scans in the binding energy region 0–1200 eV with 1.0-eV increment (step size) were recorded for G1–G6 glasses using Mg K$_\alpha$ incident photons, and as an example, a typical wide-scan XPS spectrum for the sample "G2" is shown in Fig. 1. Besides the expected main component elements Te 4d, Na 2s, Zn 3p, B 1s, Mo 3d, Te 3d, Te 3p, Zn 2p, Na 1s, and O 1s peak, a C 1s peak was also observed for the "G2" sample. This C 1s peak at 284.6 eV is caused by the hydrocarbon contamination. The XPS profile shown in Fig. 1 confirms the initial glass composition and shows the electronic configurations or the core-levels associated with "G2" glass cations. Generally, here the binding energies from 0 to ~50 eV represent electronic structure related to electrons of the outer valence molecular orbitals of the elements (Te, Zn, Na, etc.) and O 2p outer valence shells, and electrons of inner valence molecular orbitals and related to electrons of the filled low-energy valence shells for the elements including O 2s of neighboring atoms. Although the
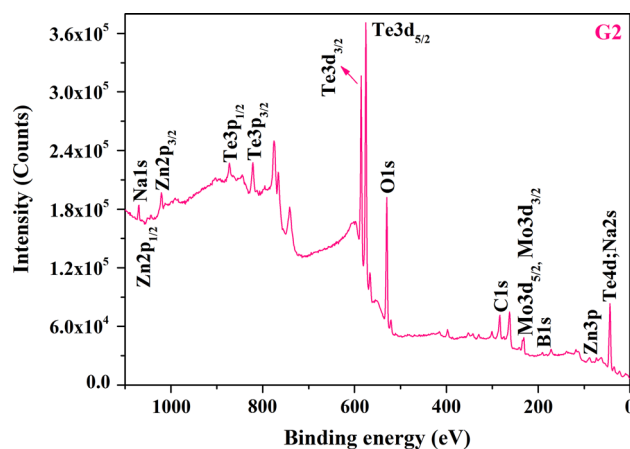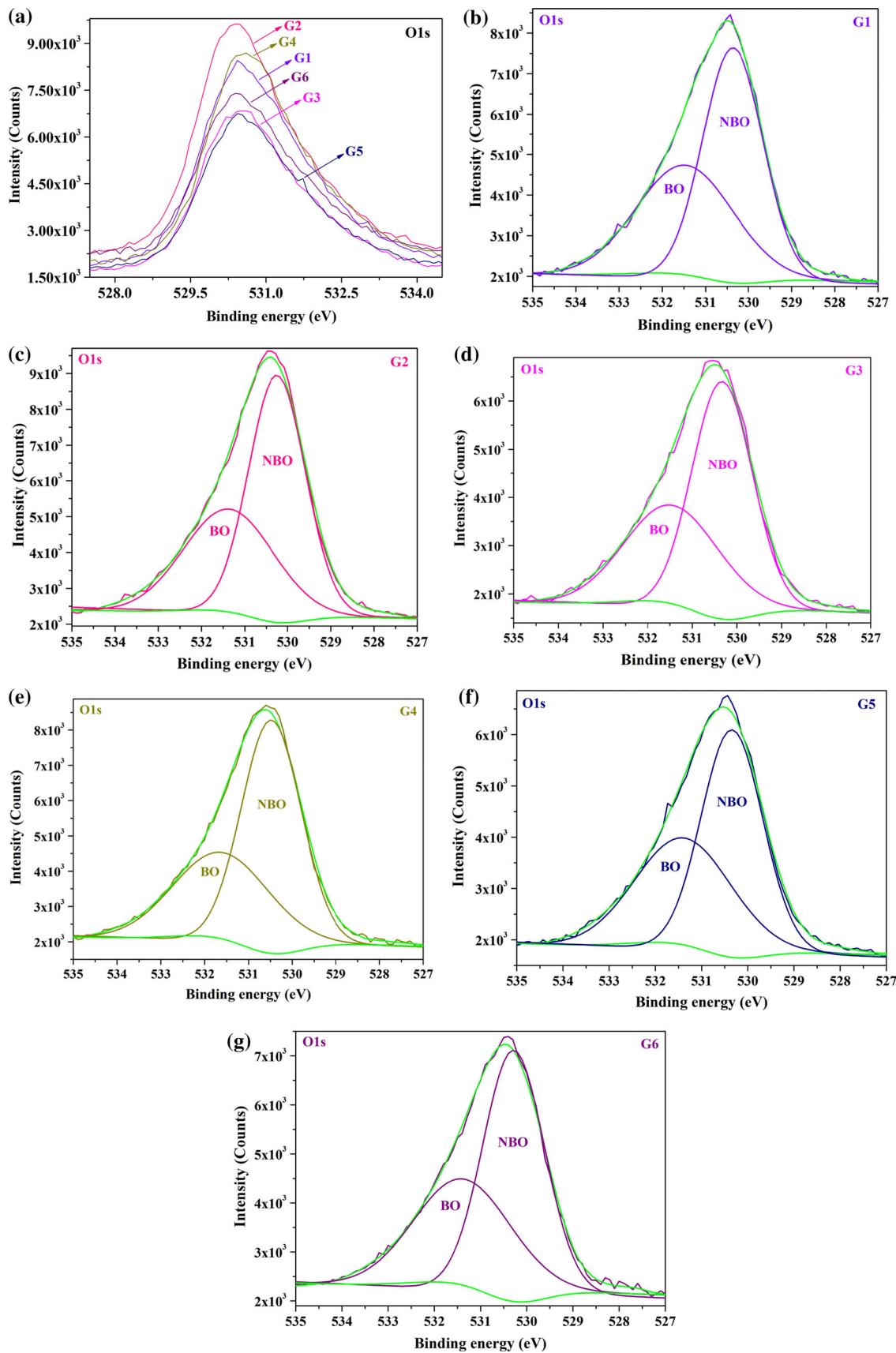

Figure 1 Wide-scan (low-resolution) XPS spectrum from the surface of the glass "G2" obtained using Mg K$_\alpha$ radiation ($hv = 1253.6$ eV).

◄ **Figure 2 a** High-resolution O1s core-level spectra for the "G1," "G2," "G3," "G4," "G5," and "G6" glasses and **b**–**g** corresponding least squares curve fitting spectra.

inclusion of alumina (Al) occurred during the glass synthesis from the crucibles used in the melting of the glass powder mixtures, which is identified by EDAX analysis [28], no peaks for aluminum were detected through the XPS studies for G1–G6 glasses. From the measured high-resolution XPS spectra of O 1s (Fig. 2a), Te 3d (Fig. 3a), Mo 3d (Fig. 4a), and Zn 2p (Fig. 5a), the peak positions of the O 1s, Te 3d, Mo 3d, and Zn 2p core-levels relative to C 1s (284.6 eV) peak and their corresponding FWHM (full width at half maximum) values for G1–G6 glasses were evaluated and the corresponding data are presented in Table 1. Here the experimental uncertainties in the spectral peak positions are less than ± 0.10 eV and for FWHM ±0.20 eV.

The XPS O 1s spectra have been successfully used to distinguish various oxygen (O) local sites and to evaluate the proportions of BO atoms and NBO atoms for various glass systems [52–57]. Figure 2a shows the high-resolution O 1s core-level spectra for G1–G6 glasses investigated in this study. The O 1s spectra show variation in peak intensity between alkali (G1, G2, and G3; G2 > G1 > G3), alkaline (G4, and G5; G4 > G5), and heavy metal oxide-added (G6) glasses in the order G2 > G4 > G1 > G6 > G3 > G5 producing more oxygen atoms in the corresponding glasses. The O 1s peak exhibits slight changes in BE values for the glass compositions (see Table 1), and the O 1s peaks for all the glasses are considerably broader as evidenced by the larger FWHM values (see Table 1). In fact, this broadening can be attributed to spectral asymmetry in the peak resulting from the appearance of a slight nonsymmetrical shape on the higher BE side of the main peak. Here, this peak asymmetry may be caused prevailingly by a change in the local oxygen environment caused by the Te atoms coordination state transformation from TeO_4 (tbp) to TeO_{3+1} polyhedron or TeO_3^- (tp) with the addition of alkali (Li, Na, and K), alkaline (Mg, Ca), or heavy metal (Pb) oxide in G1–G6 glasses [28]. (Analysis of Te $3d_{5/2}$ XPS peak has also confirmed this statement (see Fig. 3)). Since the asymmetry in the O 1s spectra could indicate the existence of more than one type of oxygen sites in the synthesized samples, for G1–G6 glasses, O 1s spectra were fitted

to two Gaussian–Lorentzian peaks by means of least squares curve fitting and are shown in Fig. 2b–g in order to determine the spectral peak positions and related FWHM values for two different oxygen sites. The BOs and NBOs show higher and lower binding energies, respectively, due to the higher effective charge on the latter. The evaluated results of these fits are displayed in Table 2 in terms of the contributions arising from a higher BE sites (designated as BO) and lower BE sites (designated as NBO). It is necessary to emphasize that the BE values are given after correction with respect to the C 1s reference. Following our previous Fourier transform infrared (FTIR) spectroscopy, and Raman structural studies on these glasses [28], here the NBO sites mainly consist of oxygen associated with Te = O, Te–O⁻M⁺, Mo–O⁻ bonds in the MoO_6 octahedral units, Zn–O bonds from ZnO_4 groups; and the BO sites with oxygen in Te–O–Te, B–O–B, Mo–O–Mo, and Te–O–Mo bonds. Further, it is reasonable to assume that the BE of these different BO type sites will be almost similar because the electronegativity (EN) value of Te, B, and Mo is identical among them (EN of Te = 2.1, B = 2.04, and Mo = 2.16) [28]. For all of the fitted O 1s spectra, the dominated peak represents NBO for all the G1–G6 glasses and NBO peak shows higher intensity than BO peak. For G1–G6 glasses, the NBO and BO peaks position varied in the BE range 530. 258 eV (G2)– 530.483 eV (G4) and 531.397 (G2)–531.693 (G4). Here it should be worth mentioning that this so-called chemical shift strongly depends on the electron space density distribution of the atoms and the higher electron density around an atom results in a lower BE of the ejected photoelectrons [58]. It is well known that usually TeO_3 unit formed in the glass structure contributes two NBOs [59]. The oxygen atoms in B–O–B and Mo–O–Mo bonds are probably more nonbridging in character compared to those in Te–O–Te units. Moreover, these rather large relative abundances of NBO indicate that MoO_3 and ZnO (both are in 10 mol %) play the role of a network modifier rather than a glass former in G1–G6 glass system. One can, in general, state that both ZnO and MoO_3 can be considered as glass formers and modifiers at higher and lower molar concentrations [28]. Generally, when alkali or alkaline and heavy metal oxides are added to the glasses, they influence the glass network structure creating more NBOs, and as an example, Sekiya et al. [60] also proposed through Raman spectroscopic studies that NBOs, which are a
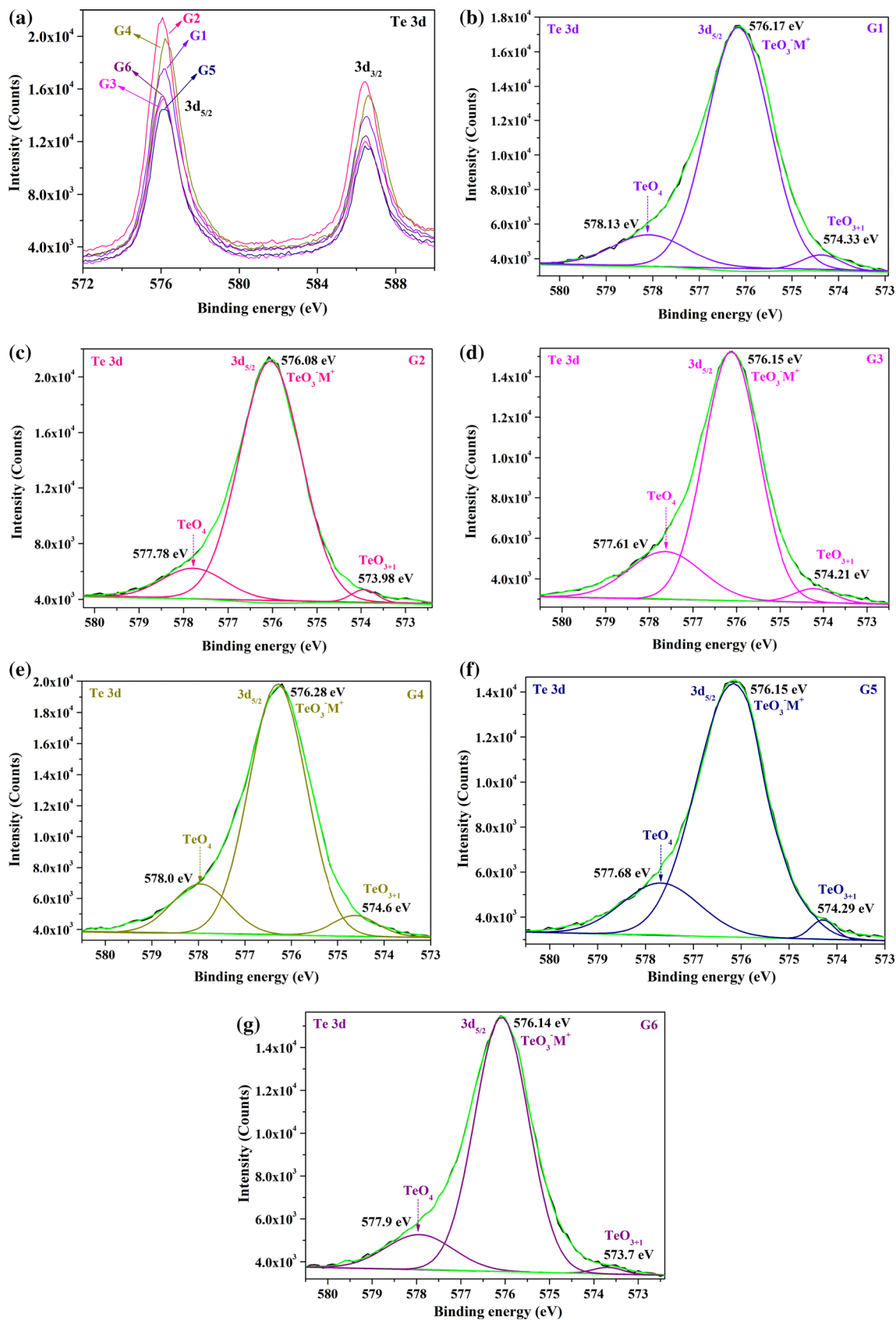
part of the TeO_{3+1} polyhedra and TeO_3 trigonal pyramid (tp) units, were formed in alkali tellurite glass system due to the addition of alkali oxides. In our study, the presence of Mo and Zn produces a more connected network than in binary tellurites. Though the role of Zn and Mo is intermediary, either as a network former (ZnO_4 and MoO_4) or as a network modifier (ZnO_6 and MoO_6) depending on their molar concentration, at lower concentrations, alkali or alkaline and heavy metal oxides and Zn in G1–G6 glasses act as modifiers, contributing to the conversion of TeO_4 to TeO_{3+1}/TeO_3 units, primarily [28]. Thus, as shown in Fig. 2 and Table 2, the O1s spectra show slight composition-dependent changes and these results indicate that, in addition to NBO atoms, also BO atoms are present in the neighborhood of Te^{4+} and B^{3+} ions.

It is well known that in crystalline form, TeO_2 possesses four coordination of Te atom, with the nearest neighbors, arranged at four vertices of a trigonal bipyramid (tbp) and a lone pair of electrons situated at the fifth position [61, 62]. Similarly, pure TeO_2 glass consists of TeO_4 trigonal bipyramids, in which one equatorial site is occupied by a lone pair of electrons and the other two equatorial and axial sites are occupied by oxygen atoms [52]. However, in TeO_2-based glasses, basic structural units of TeO_4 trigonal bipyramid (tbp), TeO_{3+1} polyhedra, TeO_3 trigonal pyramid (tp), and Te–eqOax–Te bond where the symbol "eqO" refers to an oxygen in an equatorial plane and "Oax" refers to the oxygen in an axial position with respect to the Te atom exist and the structural change of $[TeO_4](tbp) \rightarrow [TeO_{3+1}] \rightarrow [TeO_3](tp)$ takes place along with the addition of glass network modifier oxides such as alkali or alkaline and heavy metal oxides through the continuous creation of NBOs [28, 52, 60]. Also, it is well known that in glasses PbO plays the dual role, one as a modifier in PbO_6 structural units (if Pb–O is ionic) and the other as a glass former in PbO_4 structural units (if Pb–O is covalent). In Fig. 3a, we present the high-resolution Te 3d core-level spectra (spin–orbit doublet) for G1–G6 glasses and the observed higher BE peak is attributed to $Te3d_{3/2}$ and the lower BE peak is due to $Te3d_{5/2}$ [52, 63]. Following Fig. 3a, the evaluated

$Te3d_{3/2}$ and $Te3d_{5/2}$ peak positions values, FWHM, and energy separation between $Te3d_{3/2}$ and $Te3d_{5/2}$ are listed in Table 1. For G1–G6 glasses, these two peaks are varied within the BE range 586.42 eV (G2)–586.62 eV (G4) for $Te3d_{3/2}$ and 576.07 eV (G2)–576.19 (G4) eV for $Te3d_{5/2}$ (see Table 1), respectively. The FWHM values varied within the range 1.76 eV (G6)–1.88 eV (G1) and 1.72 eV (G6)–1.87 eV (G1) for $Te3d_{3/2}$ and $Te3d_{5/2}$, respectively, for G1–G6 glasses. An energy separation calculated between these $Te3d_{3/2}$ and $Te3d_{5/2}$ peaks is varied within the range 10.34 eV (G1)–10.45 eV (G6) eV for G1–G6 glass compositions. For pure TeO_2, values of 576.10, 2.07, and 10.43 eV; and 576.1, 2.1, and 10.40 eV were reported for the BE, FWHM, and spin–orbit peak separation (ΔE), respectively, following the Te 3d spectra [64, 65]. For G1–G6 glasses, the observed variations of the BE, FWHM, and ΔE of the Te 3d core-level spectra to the above reported values [64, 65] for TeO_2 suggest that there may exist different structural units for Te atom in the Li-, Na-, K-, Mg-, Ca-, or Pb oxide-added glasses. For example, Sekiya et al. [60] also proposed that in tellurite glasses, TeO_4 trigonal bipyramids (tbps) can be deformed into lower symmetry TeO_{3+1} polyhedra with the addition of alkali oxides, and further, TeO_3 trigonal pyramids (tps) form at higher alkali oxide content. Moawad et al. [66] and Mekki et al. [52] also have observed a variety of Te–O units for Te atom in silver vanadium tellurite and vanadium tellurite glasses, respectively. In order to confirm the existence of various structural units of Te (different bonding states of Te atoms) in G1–G6 glasses, the $Te3d_{5/2}$ peak XPS spectrum of each glass is tried to deconvolute into several symmetrical Gaussian functions and all of the spectra are fitted well into three bands, which are attributed to TeO_4, TeO_3^-, and TeO_{3+1} structural units [66, 67], respectively. Figure 3b–g shows the resultant deconvoluted spectra of the Te $3d_{5/2}$ peak for G1–G6 glasses, and these $Te3d_{5/2}$ deconvoluted XPS results concerning the structural evolution of the Te polyhedra in function of the chemical composition are consistent with our recently reported results of G1–G6 glasses using the Raman spectroscopy [28].

Here it should be emphasized that the TeO_3^- structural units are predominant for the G1–G6 glasses amorphous structure (Fig. 3b–g) and this can be justified due to formation of NBOs in the glasses with the presence of Zn, Mo, including addition of alkali (G1–G3) or alkaline (G4, G5) or heavy metal
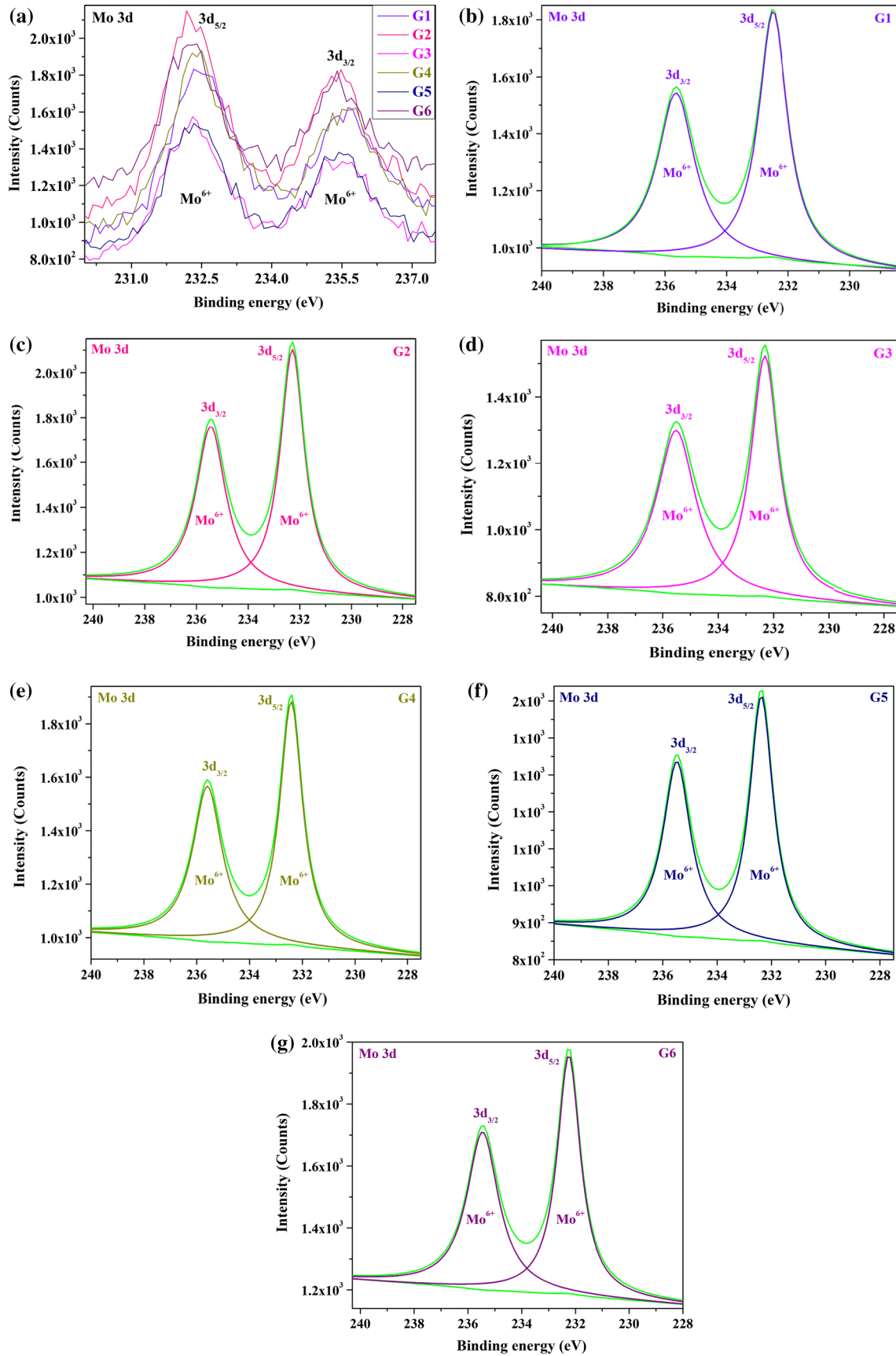
◀ **Figure 4 a** High-resolution Mo 3d core-level spectra for the "G1," "G2," "G3," "G4," "G5," and "G6" glasses and **b–g** corresponding least squares curve fitting spectra.

(G6) oxides. Figure 3b–g spectra also confirm the observed O 1s NBO strong and high-intensity peak than BO peak (Fig. 2b–g) results which are discussed earlier. In Table 3, we present the evaluated results (peak position, FWHM, and ΔE) of the deconvoluted $Te3d_{5/2}$ peak spectra for G1–G6 glasses due to the contributions arising from TeO_4, TeO_3, and TeO_{3+1} structural units of Te atom. Here the binding energy values are given after correction with respect to the C 1s reference. For G1–G6 glasses, the TeO_4, TeO_3, and TeO_{3+1} peak positions are varied in the BE range 577.61 eV (G3)–578.13 eV (G1); 576.08 (G2)–576.28 (G4); and 573.70 eV (G6)–574.60 eV (G4), respectively. The ΔE between TeO_4 and TeO_3, and TeO_3 and TeO_{3+1} structural units is varied in the range 1.46 eV (G3)–1.96 eV (G1) and 1.68 eV (G4)–2.44 eV (G6), respectively, for G1–G6 glasses. Therefore, we could conclude that the above discussion about $Te3d_{5/2}$ XPS peak corroborates our reported FTIR and Raman results of the G1–G6 (Li-, Na-, K-, Mg-, Ca-, and Pb oxide-based) glasses [28].

In order to identify the valence state of Mo ions in the G1–G6 glasses, high-resolution XPS spectra for the Mo 3d core-level were measured, and the Mo 3d spin–orbit doublet spectra for these glasses are shown in Fig. 4a. For G1–G6 glasses, the observed two peaks changed within the BEs range 232.17 eV (G2)–232.51 eV (G1) and 235.40 eV (G6)–235.68 (G1) eV (see Table 1) are assigned to the BEs of Mo $3d_{5/2}$ and Mo $3d_{3/2}$ (spin–orbit components) of Mo^{6+} ions, respectively [65]. The ΔE noticed between the Mo $3d_{5/2}$ and Mo $3d_{3/2}$ peaks is changed within the range 3.10 eV (G5)–3.31 eV (G2) eV for all the glass compositions. Recently, Pal et al. [68] have been reported the existence of Mo^{4+}, Mo^{5+}, and Mo^{6+} valence states simultaneously, for Mo ions in the MoO_3–TeO_2 glasses. In our study also, keeping in view that molybdenum (Mo) ions can exist in more than one oxidation state, each of the Mo 3d spectra was tried to fit into multiple Gaussian–Lorentzian peaks by means of least square fitting method, and the resulting fitted spectra are presented in Fig. 4b–g. As one can see from Fig. 4b–g, the fitting procedure always results in a single peak for Mo $3d_{5/2}$ spectra. Since no peaks are resolved at BEs ~ 230 eV (for Mo^{5+} state) and ~ 229 eV (for Mo^{4+} state) [65, 68] in

any of the Mo 3d spectra of G1–G6 glasses, we assume that there are no Mo^{5+}, and Mo^{4+} oxidation states present in our glasses, as the near-Gaussian shape of the Mo $3d_{5/2}$ peak indicates that most of the Mo are present in +6 charge state (Fig. 4a). Thus, the analyses of the Mo 3d spectra confirm the existence of only Mo ions in the 6+ oxidation states for all the G1–G6 glass compositions from the XPS measurements.

High-resolution Zn 2p core-level spectra for G1–G6 glasses are shown in Fig. 5a. The observed two peaks from the spin–orbit splitting of the Zn 2p core-level are attributed to $Zn2p_{3/2}$ and $Zn2p_{1/2}$ core-levels with the lower and higher BEs, respectively [55, 69]. Though the Zn 2p peak profile of core-level spectra looks similar, the variation in peak intensity was observed for G1–G6 glasses. From Fig. 5a, the evaluated $Zn2p_{3/2}$ and $Zn2p_{1/2}$ peak positions values, FWHM, and ΔE between $Zn2p_{3/2}$, and $Zn2p_{1/2}$ are given in Table 1. For G1–G6 glasses, these two peaks were changed within the BE range 1021.27 eV (G2)–1021.62 eV (G3) for $Zn2p_{3/2}$ and 1044.27 eV (G2)–1044.76 eV (G4) for $Zn2p_{1/2}$ (see Table 1), respectively. The FWHM values are varied within the range 1.50 eV (G1)–2.17 eV (G5) and 1.21 eV (G2)–3.32 eV (G1) for $Zn2p_{3/2}$ and $Zn2p_{1/2}$, respectively, for G1–G6 glasses. The ΔE calculated between these $Zn2p_{3/2}$ and $Zn2p_{1/2}$ peaks is changed within the range 22.93 eV (G3)–23.28 eV (G5) eV for G1–G6 glass compositions. Using XPS measurements, Khattak et al. [55] have been reported that pure ZnO powder exhibits Zn2p core-level doublet peaks at 1021.11 eV and 1044.18 eV, respectively, for $Zn2p_{3/2}$ and $Zn2p_{1/2}$. These two peaks showed an energy separation value of 23.07 eV and FWHM values of 2.03 eV and 2.05 eV, respectively [55]. Comparing with the ZnO powder Zn 2p core-level values, for the G1–G6 glasses the Zn 2p core-level doublet peaks are shifted in the range 0.16 eV (G2)–0.51 eV (G3) ($Zn2p_{3/2}$) and 0.09 eV (G2)–0.58 eV (G4) ($Zn2p_{1/2}$) toward higher BEs and this could be possibly due to the presence of different molecular environments [56], formed by other glass components (TeO_2, B_2O_3, MoO_3) complex network structures that exist around Zn atom in the glasses with the addition of Li, Na, K, Mg, Ca, and Pb oxides.

In order to verify the various molecular coordinations that exist around Zn atom in G1–G6 glasses, the slight asymmetric $Zn2p_{3/2}$ peak XPS spectrum of each glass is deconvoluted and fitted well into three symmetric Gaussian functions, and Fig. 5b–g
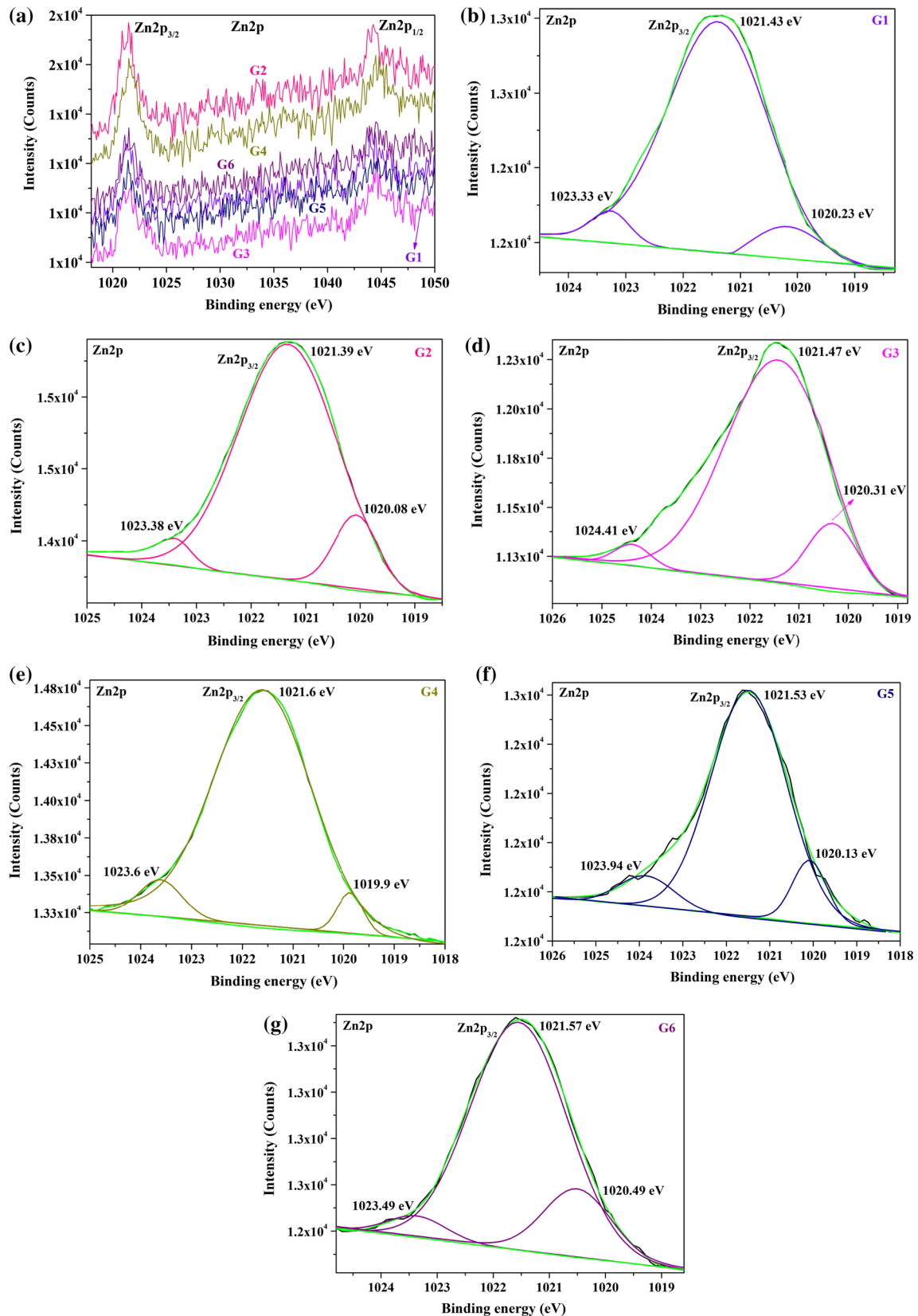
Figure 5 **a** High-resolution Zn 2p core-level spectra for the "G1," "G2," "G3," "G4," "G5," and "G6" glasses and **b–g** corresponding deconvoluted Zn $2p_{3/2}$ peak spectra.

Table 1 Peak positions (in eV) relative to C 1s (284.6 eV) and their corresponding FWHM (full width at half maximum) given in the parenthesis for the core-levels Te 3d, Zn 2p, Mo 3d, and O 1s of "G1," "G2," "G3," "G4," "G5," and "G6" glasses

Sample code	Te 3d$_{5/2}$ (FWHM)	Te 3d$_{3/2}$ (FWHM)	ΔE Te 3d	Zn 2p$_{3/2}$ (FWHM)	Zn 2p$_{1/2}$ (FWHM)	ΔE Zn 2p	Mo 3d$_{5/2}$ (FWHM)	Mo 3d$_{3/2}$ (FWHM)	ΔE Mo 3d	O 1s (FWHM)
G1	576.16 (1.87)	586.50 (1.88)	10.34	1021.34 (1.50)	1044.48 (3.32)	23.14	232.51 (1.78)	235.68 (1.34)	3.17	530.43 (2.26)
G2	576.07 (1.73)	586.42 (1.79)	10.35	1021.27 (1.71)	1044.27 (1.21)	23.00	232.17 (1.56)	235.48 (1.27)	3.31	530.41 (2.18)
G3	576.11 (1.76)	586.46 (1.84)	10.35	1021.62 (1.91)	1044.55 (2.34)	22.93	232.32 (1.59)	235.53 (1.32)	3.21	530.54 (2.27)
G4	576.19 (1.77)	586.62 (1.84)	10.43	1021.55 (1.92)	1044.76 (2.19)	23.21	232.41 (1.54)	235.61 (1.55)	3.20	530.60 (2.25)
G5	576.15 (1.79)	586.58 (1.77)	10.43	1021.42 (2.17)	1044.70 (3.11)	23.28	232.34 (1.42)	235.44 (1.40)	3.10	530.48 (2.23)
G6	576.09 (1.72)	586.54 (1.76)	10.45	1021.49 (1.69)	1044.62 (1.98)	23.13	232.28 (1.34)	235.40 (1.10)	3.12	530.41 (2.30)

shows the curve fitting of the Zn2p$_{3/2}$ photoelectron peak. Here the high-intensity band is related to Zn bonded to oxygen with BEs of 1021.43 eV, 1021.39 eV, 1021.47 eV, 1021.60 eV, 1021.53 eV, and 1021.57 eV for "G1," "G2," "G3," "G4," "G5," and "G6" glasses, respectively, and the other two side components could be related to more complex structures formed inside the glass matrices. Though in oxide glasses, the zinc atoms are usually bonded to four oxygen atoms, the addition of Li, Na, K, Mg, Ca, and Pb oxides should induce changes (creating NBOs) in the zinc molybdenum borotellurite glass network structure acting as modifiers. As a result, the 2p core-level spectra of zinc are formed by three bands. Therefore, here we should state that probably in G1–G6 glasses, there is a considerable percentage (around 20–30%) of zinc that is not described by a simple single bond with four oxygen atoms. Previously, Speranza et al. [56] and Medda et al. [70] have also reported that in oxide glasses Zn can possess a coordination number different from four such as in borate [56] and phosphate [70] glasses, respectively. Thus, different mutual interactions between tellurium, boron, and zinc ions mediated by oxygen atoms could explain the presence of the two zinc side bands or components in the 2p$_{3/2}$ peak fitting as the ability of the Zn cation to accommodate six oxygen neighbors, when more oxygen atoms (say, NBO) are available, was earlier reported in the literature [71].

Radiation shielding parameters of G1–G6 glasses

Mass attenuation coefficients

Figure 6 shows the mass attenuation coefficients (μ/ρ) for the selected borotellurite glasses for the incident photon energy from 1 keV to 100 GeV. From Fig. 6, it is observed that the μ/ρ values for all the samples initially decrease very sharply and then slowly and finally again increase to become nearly constant. Therefore, this variation has been divided into three regions as low-, intermediate-, and high-energy regions and can be explained using different partial photon interaction processes.

In the low-energy region (E < 200 keV), the μ/ρ value reduces very sharply due to the photoelectric effect. Since the photoelectric interaction cross section is proportional to $Z^{4-5}/E^{3.5}$, results are in dominance for an atomic number of elements as well as

Table 2 Peak positions and FWHM of NBO and BO including ΔE_{BO-NBO} (eV) resulting from the curve fitting of the O 1s core-level for the G1–G6 glasses

Sample code	O 1s (BE) (eV)		FWHM (eV)		ΔE_{BO-NBO} (eV)
	NBO	BO	NBO	BO	
G1	530.378	531.518	1.649	2.522	1.140
G2	530.258	531.397	1.554	2.354	1.139
G3	530.350	531.512	1.589	2.396	1.162
G4	530.483	531.693	1.611	2.419	1.210
G5	530.326	531.447	1.545	2.328	1.121
G6	530.282	531.424	1.544	2.328	1.142

Table 3 Peak positions and FWHM of TeO_{3+1}, TeO_3, and TeO_4 including ΔE (TeO_4–TeO_3) (eV), ΔE (TeO_3–TeO_{3+1}) (eV) resulting from the deconvolution of the Te $3d_{5/2}$ peak for the G1–G6 glasses

Sample code	Te$3d_{5/2}$ (TeO$_4$)		Te$3d_{5/2}$ (TeO$_3$)		Te$3d_{5/2}$ (TeO$_{3+1}$)		ΔE (TeO$_4$–TeO$_3$) (eV)	ΔE (TeO$_3$–TeO$_{3+1}$) (eV)
	Position (eV)	FWHM (eV)	Position (eV)	FWHM (eV)	Position (eV)	FWHM (eV)		
G1	578.13	1.75	576.17	1.59	574.33	0.95	1.96	1.84
G2	577.78	1.58	576.08	1.62	573.98	0.65	1.70	2.10
G3	577.61	1.94	576.15	1.47	574.21	0.96	1.46	1.94
G4	578.00	1.39	576.28	1.45	574.60	1.06	1.72	1.68
G5	577.68	1.81	576.15	1.67	574.29	0.58	1.53	1.86
G6	577.90	1.70	576.14	1.42	573.70	0.61	1.76	2.44

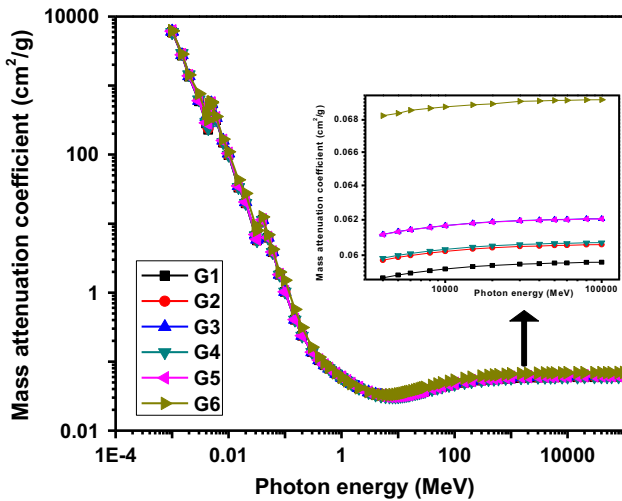**Figure 6** Mass attenuation coefficients for the G1–G6 glasses for total interaction from 1 to 100 GeV.

Figure 7 Effective atomic numbers for the G1–G6 glasses for total interaction from 1 to 100 GeV.

reduction with the increment of incident photon energy. In the intermediate energy region (200 keV $< E <$ 5 MeV), the values of μ/ρ vary slowly because photon goes under Compton scattering process where incoherent scattering is linearly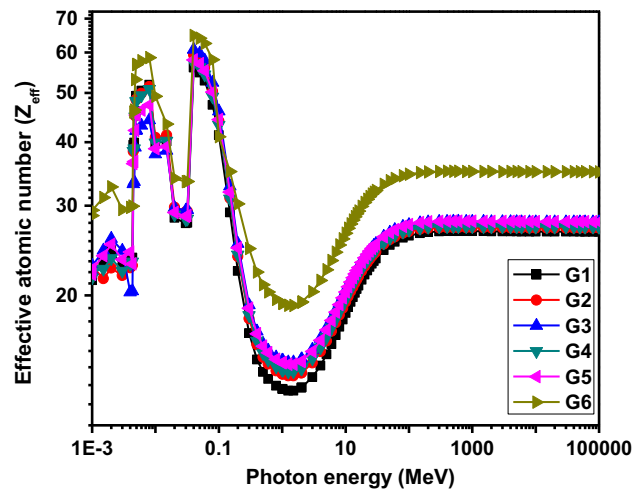 proportional to Z. In the high-energy region, μ/ρ values increase, where the pair production is significant as cross section is dependent upon Z^2.
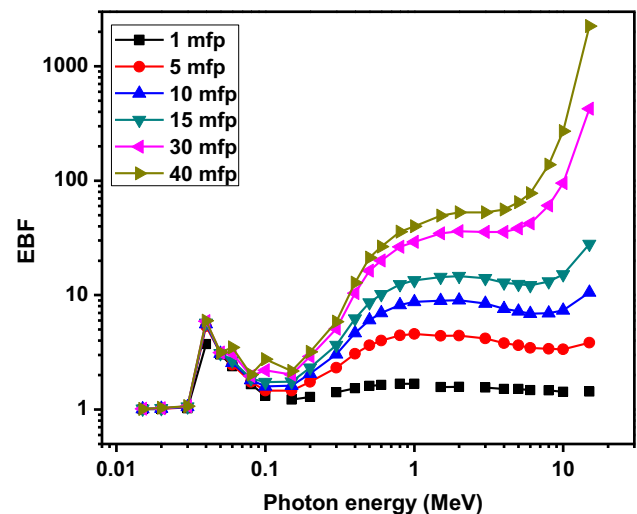
Also, in the low-energy region, different sharp edges can be observed which may be due to

Table 4 Equivalent atomic number for G1–G6 glasses

Energy (MeV)	G1	G2	G3	G4	G5	G6
0.015	21.772	21.900	22.350	21.892	22.329	24.381
0.02	23.965	24.066	24.433	24.046	24.413	27.432
0.03	24.567	24.631	24.940	24.615	24.930	28.029
0.04	38.783	38.829	39.001	38.786	38.948	40.911
0.05	39.366	39.379	39.531	39.342	39.498	41.404
0.06	39.799	39.799	39.923	39.761	39.899	41.757
0.08	40.333	40.319	40.429	40.282	40.393	42.236
0.1	40.698	40.678	40.766	40.638	40.741	47.452
0.15	41.225	41.190	41.272	41.156	41.244	48.342
0.2	41.522	41.498	41.562	41.462	41.527	48.867
0.3	41.894	41.850	41.893	41.829	41.885	49.494
0.4	42.082	42.057	42.076	41.997	42.040	49.902
0.5	42.199	42.145	42.197	42.126	42.169	50.137
0.6	42.256	42.236	42.283	42.203	42.235	50.293
0.8	42.316	42.313	42.340	42.241	42.349	50.468
1	42.408	42.368	42.359	42.339	42.331	50.560
1.5	40.894	40.955	40.936	40.785	41.013	49.322
2	37.120	37.228	37.571	37.168	37.613	45.838
3	33.398	33.723	34.332	33.706	34.269	41.256
4	32.112	32.467	33.153	32.425	33.081	39.445
5	31.508	31.886	32.609	31.835	32.537	38.492
6	31.118	31.499	32.243	31.431	32.127	37.956
8	30.628	31.005	31.759	30.991	31.655	37.253
10	30.441	30.842	31.584	30.785	31.491	36.945
15	30.312	30.722	31.498	30.730	31.420	36.721
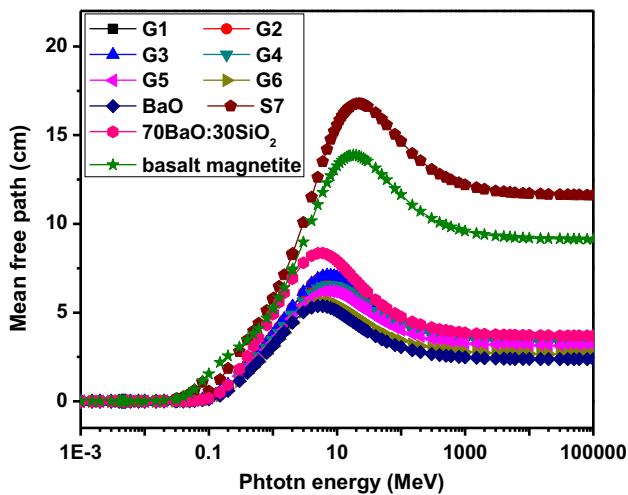
Figure 8 Mean free path (MFP) of the selected glasses as a function of photon energy in comparison with some standard shielding materials.

Figure 9 Variation in exposure buildup factors with energy for G6 (as an example) with photon energy at selected penetration depths 1, 5, 10, 15, 30, and 40 mfp.

absorption edges of K, L, M shell electrons of the elements (Na, K, Mg, Ca, Zn, Mo, Te, and Pb). Figure 6 shows that the μ/ρ values for sample "G6,"

which contains high Z-element (i.e., Pb), are the largest among the selected glasses while sample G1 shows the minimum values. The largest values of μ/ρ
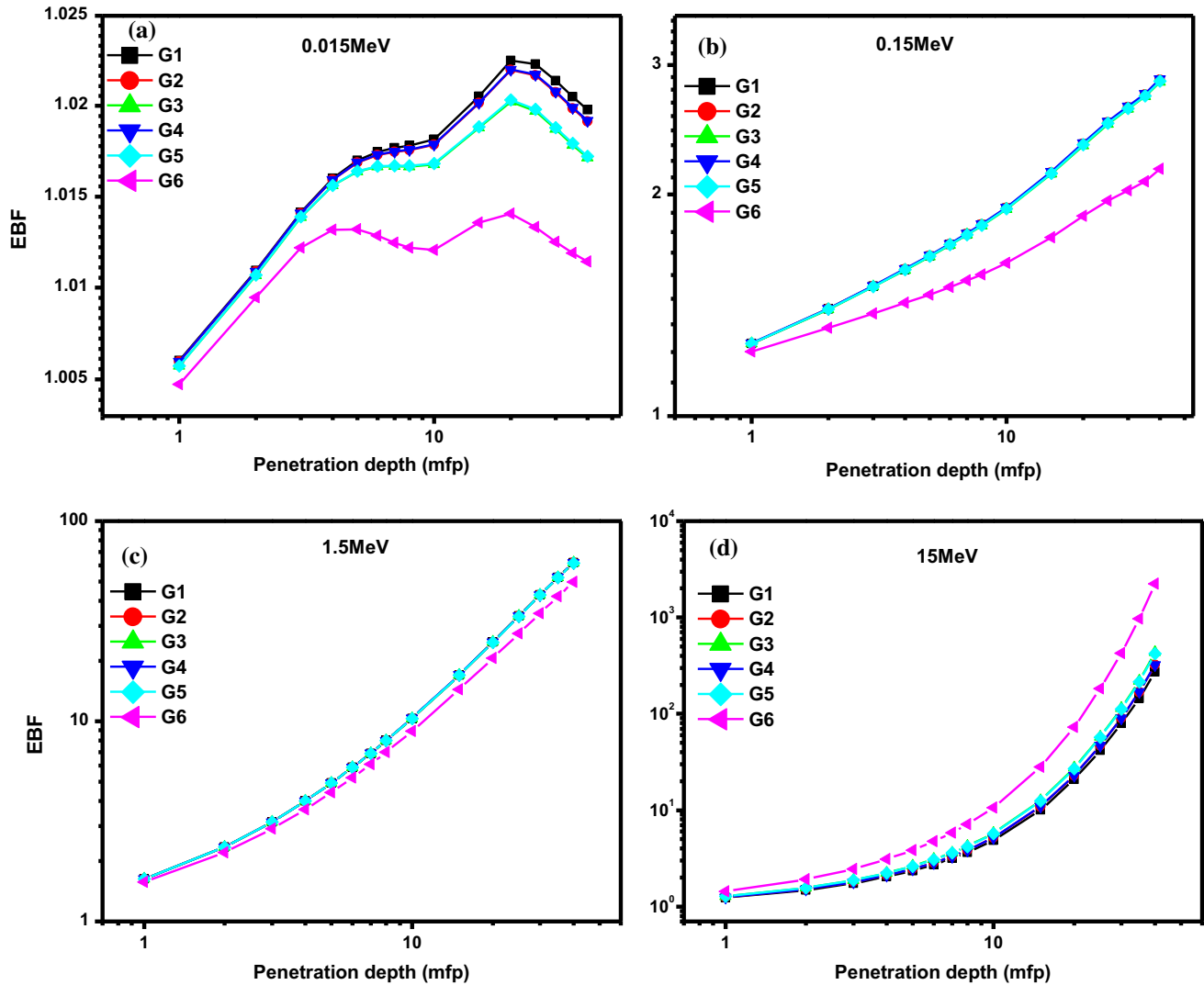
Figure 10 Variation in exposure buildup factors for the G1–G6 glasses with penetration depth at selected energies 0.015, 0.15, 1.5, and 15 MeV.

signify that the removal of the photon from the materials is the highest. Therefore, sample "G6" provides superior gamma-ray shielding effectiveness.

Effective atomic number

The variation of Z_{eff} with the incident photon energy for all samples G1–G6 is shown in Fig. 7. As in the case of mass attenuation coefficients, this figure also shows the dominance of several interaction processes in different energy regions. Obviously, it can be seen that the values of Z_{eff} depend on the modifier oxides in the studied glasses and incident photon energy. With changing of the modifier oxides, the values of Z_{eff} increase or decrease, which indicates the

significance of selection of certain oxides for required radiation shielding applications. It is also noted that in the low-energy region, two sudden jumps occurred at 4 and 40 keV, and these jumps can be explained on the basis of absorption edges of Te. The incident photon energy corresponding to L- and K-absorption edge of Te appears at the incident photon energy L3 (4.34 keV), L2 (4.61 keV), L1 (4.94 keV), and K (31.18 keV). Additionally, it can be observed that in the moderate energy region (0.4–5 MeV), the minimum value of Z_{eff} is found. Beyond 5 MeV, the Z_{eff} increases with an increment in energy, and at incident photon energy 60 MeV, the Z_{eff} value becomes nearly constant. It was observed that among the selected G1–G6 glass samples, the Z_{eff}

Table 5 EBF for all the G1–G6 glasses at different penetration depths and different energies

Energy (MeV)	G1	G2	G3	G4	G5	G6
(a) Exposure buildup factor for 1 mfp						
0.015	1.01	1.01	1.01	1.01	1.01	1.01
0.15	1.26	1.27	1.25	1.26	1.26	1.22
1.5	1.63	1.63	1.63	1.63	1.63	1.57
15	1.24	1.25	1.28	1.25	1.27	1.43
(b) Exposure buildup factor for 5 mfp						
0.015	1.02	1.02	1.02	1.02	1.02	1.01
0.15	1.65	1.65	1.65	1.65	1.65	1.46
1.5	4.91	4.91	4.91	4.92	4.91	4.41
15	2.36	2.45	2.63	2.45	2.61	3.85
(b) Exposure buildup factor for 10 mfp						
0.015	1.02	1.02	1.02	1.02	1.02	1.01
0.15	1.92	1.92	1.91	1.92	1.91	1.62
1.5	10.34	10.33	10.33	10.35	10.32	8.93
15	4.84	5.16	5.77	5.16	5.71	10.57
(c) Exposure buildup factor for 20 mfp						
0.015	1.02	1.02	1.02	1.02	1.02	1.01
0.15	2.34	2.35	2.33	2.35	2.34	1.87
1.5	24.84	24.82	24.83	24.88	24.80	20.65
15	20.77	22.97	27.52	23.02	27.04	73.07
(e) Exposure buildup factor for 40 mfp						
0.015	1.02	1.02	1.02	1.02	1.02	1.01
0.15	2.86	2.87	2.85	2.87	2.85	2.17
1.5	61.87	61.80	61.82	61.99	61.74	49.54
15	272.73	321.71	433.14	322.72	420.67	2240.15

Table 6 Values of effective removal cross sections $\sum_R$ (cm^{-1}) for the G1–G6 glasses

	Samples					
	G1	G2	G3	G4	G5	G6
$\sum_R$(cm^{-1})	0.1273	0.1099	0.1047	0.1191	0.1204	0.1183

of sample G6 was the largest (since it contains the highest atomic number constituent element, i.e., lead), which means that it absorbs effectively incident photons; therefore, it has been shown with the highest gamma-ray shielding competence, whereas the Z_{eff} values for sample G1 were found lower than for all other samples. Hence, it has weak gamma-ray shielding property. The equivalent atomic number values for G1–G6 glasses in the energy region 0.015–15 MeV are presented in Table 4.

Mean free path

Mean free path (MFP) has been compared between samples G1–G6 including literature values for some

standard shielding glasses and basalt magnetite concrete [72–75] as shown in Fig. 8. From Fig. 8, it is obvious that the values of MFP are very small for $E < 0.1$ MeV and the values of MFP for samples G1–G6 increase rapidly thereafter and reach a maximum at about 10 MeV. Also, it can be observed from Fig. 8 that for incident photon energy higher than 200 MeV the MFP values are almost constant. It is observed that all samples G1–G6 have lower values of MFP than S7, basalt–magnetite concrete, and 70 BaO: 30 SiO$_2$. In light of these results, we can conclude that our glasses studied in this work possess better shielding properties than some standard shielding glasses and basalt–magnetite concrete.

Exposure buildup factor (EBF)

The variation in exposure buildup factors for sample G6 (as an example) with the photon energy at selected penetration depths 1, 5, 10, 15, 30, and 40 mfp is shown in Fig. 9. Similar plots with same features were obtained for the G1–G5 glasses also and are not shown here. From Fig. 9, it can be seen that the EBF

values for all the penetration depths are about one in the low-energy region and the sudden jump occurs at 40 keV which could be attributed to k-edge absorption of Te at 31.18 keV. Also, the EBF values increase with an increase in the mean free path of the glass. This behavior of EBF profile shows that more photon buildups for large penetration depths and high-energy photons. The variation for EBF can be explained by photon interaction process similar to mass attenuation coefficients.

Variation of the EBF for the samples G1–G6 with penetration depth (0–40 mfp) is shown in Fig. 10a–d. The EBF values for all the G1–G6 glasses at different penetration depths and different energies are shown in Table 5. It is worth mentioning that the EBF for the glass samples increases with photon energy and penetration depth. At incident photon energy 0.015 MeV (Fig. 10a), the EBF values for the glass samples G1–G6 were found to be in the range of 1.004–1.011 with the lowest for sample G6 (which possesses the highest Z_{eq}). As the photon energy increases (Fig. 10b–c), the values of EBF almost remain the same for all the penetration depths for samples G1–G5 and the lowest EBF was observed again for sample G6 for the penetration depth range 0–40 mfp. From Fig. 10d, one can see the reverse behavior of the dependence of EBF in Z_{eq}, i.e., the highest Z_{eq} (sample G6) show the largest EBF. This can be explained by the formation of electron and positron pairs in high-energy region (pair production region). The positron at rest annihilates with an electron to produce secondary photons of equal energies (0.511 MeV). In low penetration depths, these photons can pass through the glass samples, whereas multiple scattering will occur for the large penetration depths.

Effective removal cross section of fast neutrons

The effective fast neutron removal cross sections ($\sum_R$, cm^{-1}) for the different glasses were calculated using Eq. (4), and the results are presented in Table 6. It is found that the $\sum_R$ value slightly higher for the sample G1 and the minimum values were recorded for sample G3, and this leads to the conclusion that sample G1 is more effective and suitable for neutron radiation shielding than the other samples. An elevated value of $\sum_R$ for sample G1 can be attributed to the lithium (Li, light element) which has a high value of mass removal cross section compared to other

elements ($\sum_R/\rho = 0.084$ cm^2 g^{-1}). We found that Σ_R (cm^{-1}) for sample G1 is in an order of experimental values of basalt–magnetite and Σ_R for all samples G1–G6 were higher than the ordinary concrete, haematite–serpentine, and ilmenite–limonite [72]. In addition, we found that Σ_R (cm^{-1}) for sample G5 is equal to TeO_2–B_2O_3 glass composition Σ_R (cm^{-1}) value [75].

Conclusions

In summary, transparent and stable zinc molybdenum borotellurite glasses containing various network modifiers have been fabricated by melt quenching technique and their local environment around O, Te, Mo, and Zn atoms (using XPS measurements) was investigated. The O 1s core-level XPS spectra indicate the BO atoms in Te–O–Te, B–O–B, Te–O–Mo, and Mo–O–Mo configurations at a slightly higher BE than the NBO atoms in the Te = O, Te–O$^-$M$^+$, Mo–O$^-$ bonds in the MoO_6 octahedral units, and Zn–O bonds from ZnO_4 configurations. The Te 3d XPS spectra for the glasses showed the presence of different structural units of the tellurium atom, and the coordination of the Te atom changes from 4 to 3, which leads to the formation of TeO_4, TeO_3^-, and TeO_{3+1} units, respectively. The study of the Mo 3d XPS spectra indicates the existence of Mo ions in the 6+ oxidation state for the glass compositions. The Zn 2p core XPS spectra show that zinc is mainly coordinated by four oxygen atoms. However, the zinc $2p_{3/2}$ photoelectron peak shows the presence of oxygen atoms which mediate the interaction among tellurium, boron, and zinc atoms. The Zn $2p_{3/2}$ peak shifted to higher BE side in comparison with standard ZnO powder, probably due to the changes in the chemical environment in the glasses complex network structures that exist around Zn atom. Both B_2O_3 and TeO_2 play network formers role, MoO_3 and ZnO mainly act as network modifiers, and by comparison, the Te and Zn XPS valence band spectra show significant systematic changes that were consistent with the variation of chemical composition in the glasses. All the selected alkali or alkaline and heavy metal oxides entered the glass structure as network modifiers. Further, the radiation shielding parameters such as mass attenuation coefficient, effective atomic number, mean free path, exposure buildup factor, and macroscopic effective removal cross section ($\sum_R$) for fast neutrons of the synthesized glasses were

investigated using WinXCom program. Among the studied glasses, PbO-introduced glass shows the best gamma-ray shielding properties due to its higher values for mass attenuation coefficient, effective atomic number, and lower values of both MFP and EBF. The obtained results of the glasses were compared in terms of the mean free path with different shielding glasses and basalt–magnetite concrete.

Acknowledgements

References

[1] Arbuzov VI, Nikonorov NV (2013) Neodymium, erbium and ytterbium laser glasses, chapter 5. In: Denker B, Shklovsky E (eds) Handbook of solid-state lasers: materials, systems and applications. A volume in Woodhead publishing series in electronic and optical materials. Woodhead Publishing Limited, Elsevier, Cambridge, pp 110–138

[2] Tanabe S (2002) Rare-earth-doped glasses for fiber amplifiers in broadband telecommunication. C R Chim 5:815–824

[3] Jayasimhadri M, Jang K, Lee HS, Chen B, Yi S-S, Jeong J-H (2009) White light generation from Dy^{3+}-doped ZnO–B_2O_3–P_2O_5 glasses. J Appl Phys 106:013105

[4] Chen B, Shen L, Lin H, Pun EYB (2011) Signal amplification in rare-earth doped heavy metal germanium tellurite glass fiber. J Opt Soc Am B 28:2320–2327

[5] Xia F, Liu S, Wang Y, Mao J, Li X, Wang Y, Chen G (2015) Fast and intense green emission of Tb^{3+} in borosilicate glass modified by Cu^+. Sci Rep 5:1–7

[6] Lu Y, Cai M, Cao R, Qian S, Xu S, Zhang J (2016) Er^{3+} doped germanate–tellurite glass for mid-infrared 2.7 μm fiber laser material. J Quant Spectrosc Radiat Trans 171: 73–81

[7] Guo H, Wang Y, Gong Y, Yin H, Mo Z, Tang Y, Chi L (2016) Optical band gap and photoluminescence in heavily Tb^{3+} doped GeO_2–B_2O_3–SiO_2–Ga_2O_3 magneto-optical glasses. J Alloys Compd 686:635–640

[8] Pisarski WA, Pisarska J, Dominiak-Dzik G, Ryba-Romanowski W (2004) Visible and infrared spectroscopy of Pr^{3+} and Tm^{3+} ions in lead borate glasses. J Phys Condens Matter 16:6171–6184

[9] Rajesh D, Ratnakaram YC, Seshadri M, Balakrishna A (2012) Luminescence properties of Sm^{3+} impurities in

[10] Annapoorani K, Basavapoornima Ch, Suriya Murthy N, Marimuthu K (2016) Investigations on structural and luminescence behavior of Er^{3+} doped Lithium Zinc borate glasses for lasers and optical amplifier applications. J Non-Cryst Solids 447:273–282

[11] Pawar PP, Munishwar SR, Gedam RS (2016) Physical and optical properties of Dy^{3+}/Pr^{3+} co-doped lithium borate glasses for W-LED. J Alloys Compd 660:347–355

[12] Oermann MR, Ebendorff-Heidepriem H, Li Y, Foo T-C, Monro TM (2009) Index matching between passive and active tellurite glasses for use in microstructured fiber lasers: erbium doped lanthanum–tellurite glass. Opt Express 17:15578–15584

[13] Feng X, Shi J, Segura M, White NM, Kannan P, Calvez L, Zhang X, Brilland L, Loh WH (2013) Towards water-free tellurite glass fiber for 2–5 μm nonlinear applications. Fibers 1(3):70–81

[14] Shen S, Jha A, Liu X, Naftaly M, Bindra K, Bookey HJ, Kar AK (2002) Tellurite glasses for broadband amplifiers and integrated optics. J Am Ceram Soc 85:1391–1395

[15] Madden SJ, Vu KT (2012) High-performance integrated optics with tellurite glasses: status and prospects. Int J Appl Glass Sci 3:289–298

[16] Toney Fernandez T, Hernandez M, Sotillo B, Eaton SM, Jose G, Osellame R, Jha A, Fernandez P, Solis J (2014) Role of ion migrations in ultrafast laser written tellurite glass waveguides. Opt Express 22:15298–15304

[17] Desirena H, Schulzgen A, Sabet S, Ramos-Ortiz G, de la Rosa E, Peyghambarian N (2009) Effect of alkali metal oxides R_2O (R = Li, Na, K, Rb and Cs) and network intermediate MO (M = Zn, Mg, Ba and Pb) in tellurite glasses. Opt Mater 31:784–789

[18] Lakshminarayana G, Kaky KM, Baki SO, Ye S, Lira A, Kityk IV, Mahdi MA (2016) Concentration dependent structural, thermal, and optical features of Pr^{3+}-doped multicomponent tellurite glasses. J Alloys Compd 686:769–784

[19] Rada S, Culea M, Culea E (2008) Structure of $TeO_2 \cdot B_2O_3$ glasses inferred from infrared spectroscopy and DFT calculations. J Non-Cryst Solids 354:5491–5495

[20] Maheshvaran K, Marimuthu K (2012) Concentration dependent Eu^{3+} doped boro-tellurite glasses—Structural and optical investigations. J Lumin 132:2259–2267

[21] Kaur N, Khanna A, Krishna PSR (2014) Preparation and characterization of boro-tellurite glasses. AIP Conf Proc 1591:802–804

[22] Pandarinath MA, Upender G, Rao KN, Babu DS (2016) Thermal, optical and spectroscopic studies of boro-tellurite glass system containing ZnO. J Non-Cryst Solids 433:60–67

strontium lithium bismuth borate glasses. AIP Conf Proc 1447:581–582

[23] Mahraz ZAS, Sahar MR, Ghoshal SK (1072) Band gap and polarizability of boro-tellurite glass: influence of erbium ions. J Mol Struc 2014:238–241

[24] Azlan MN, Halimah MK, Shafinas SZ, Daud WM (2015) Electronic polarizability of zinc borotellurite glass system containing erbium nanoparticles. Mater Express 5:211–218

[25] Chung WJ, Park BJ, Seo HS, Ahn JT, Choi YG (2006) Spontaneous Raman scattering bandwidth broadening of tellurite glasses with MoO_3 or WO_3. Chem Phys Lett 419:400–404

[26] Chung WJ, Choi YG (2010) 1.4 μm emission properties and local environments of Tm_{3+} ions in tellurite glass modified with MoO_3. J Lumin 130:2175–2179

[27] Yuan J, Yang Q, Chen DD, Qian Q, Shen SX, Zhang QY, Jiang ZH (2012) Compositional effect of WO_3, MoO_3, and P_2O_5 on Raman spectroscopy of tellurite glass for broadband and high gain Raman amplifier. J Appl Phys 111:103511-1–103511-6

[28] Lakshminarayana G, Kaky KM, Baki SO, Lira A, Nayar P, Kityk IV, Mahdi MA (2017) Physical, structural, thermal, and optical spectroscopy studies of TeO_2–B_2O_3–MoO_3–ZnO–R_2O (R = Li, Na, and K)/MO (M = Mg, Ca, and Pb) glasses. J Alloys Compd 690:799–816

[29] Barney ER, Hannon AC, Holland D, Umesaki N, Tatsumisago M (2015) Alkali environments in tellurite glasses. J Non-Cryst Solids 414:33–41

[30] Leal JJ, Narro-García R, Desirena H, Marconi JD, Rodríguez E, Linganna K, De la Rosa E (2015) Spectroscopic properties of tellurite glasses co-doped with Er_{3+} and Yb_{3+}. J Lumin 162:72–80

[31] Sayyed MI, Qashou SI, Khattari ZY (2017) Radiation shielding competence of newly developed TeO_2–WO_3 glasses. J Alloys Compd 696:632–638

[32] Matori KA, Sayyed MI, Sidek HAA, Zaid MHM, Singh VP (2017) Comprehensive study on physical, elastic and shielding properties of lead zinc phosphate glasses. J Non-Cryst Solids 457:97–103

[33] Waly ESA, Fusco MA, Bourham MA (2016) Gamma-ray mass attenuation coefficient and half value layer factor of some oxide glass shielding materials. Ann Nucl Energy 96:26–30

[34] Kaur K, Singh KJ, Anand V (2016) Structural properties of Bi_2O_3–B_2O_3–SiO_2–Na_2O glasses for gamma ray shielding applications. Radiat Phys Chem 120:63–72

[35] Chanthima N, Kaewkhao J (2013) Investigation on radiation shielding parameters of bismuth borosilicate glass from 1 keV to 100 GeV. Ann Nucl Energy 55:23–28

[36] Singh K, Singh H, Sharma G, Gerward L, Khanna A, Kumar R, Nathuram R, Sahota HS (2005) Gamma-ray shielding properties of CaO–SrO–B_2O_3 glasses. Radiat Phys Chem 72:225–228

[37] Singh KJ, Kaur S, Kaundal RS (2014) Comparative study of gamma ray shielding and some properties of PbO–SiO_2–Al_2O_3 and Bi_2O_3–SiO_2–Al_2O_3 glass systems. Radiat Phys Chem 96:153–157

[38] Gerward L, Guilbert N, Jensen KB, Levring H (2004) WinXCom—a program for calculating X-ray attenuation coefficients. Radiat Phys Chem 71:653–654

[39] Manohara SR, Hanagodimath SM, Thind KS, Gerward L (2010) The effective atomic number revisited in the light of modern photon-interaction cross-section databases. Appl Radiat Isot 68:784–787

[40] Manohara SR, Hanagodimath SM (2007) Studies on effective atomic numbers and electron densities of essential amino acids in the energy range 1 keV–100 GeV. Nucl Instrum Methods Phys Res B 258:321–328

[41] Sayyed MI (2017) Half value layer, mean free path and exposure buildup factor for tellurite glasses with different oxide compositions. J Alloys Compd. 695:3191–3197

[42] Mavi B (2012) Experimental investigation of γ-ray attenuation coefficients for granites. Ann Nucl Energy 44:22–25

[43] Sayyed MI, Elmahroug Y, Elbashir BO, Issa SAM (2016) Gamma-ray shielding properties of zinc oxide soda lime silica glasses. J Mater Sci Mater Electron. doi:10.1007/s10854-016-6022-z

[44] Sayyed MI, Elhouichet H (2017) Variation of energy absorption and exposure buildup factors with incident photon energy and penetration depth for boro-tellurite (B_2O_3–TeO_2) glasses. Radiat Phys Chem 130:335–342

[45] Issa S, Sayyed M, Kurudirek M (2016) Investigation of gamma radiation shielding properties of some zinc tellurite glasses. J Phys Sci 27:97–119

[46] Elmahroug Y, Tellili B, Souga C (2014) Determination of shielding parameters for different types of resins. Ann Nucl Energy 63:619–623

[47] Profio AE (1979) Radiation shielding and dosimetry. Wiley, New York

[48] Chilton AB, Shultis JK, Faw RE (1984) Principles of radiation shielding. Prentice-Hall, Englewood Cliffs

[49] Rivero C (2005) High gain/broadband oxide glasses for next generation Raman amplifiers". Ph.D Thesis, University of Central Florida, USA. http://stars.library.ucf.edu/etd/611

[50] McGuire GE, Schweitzer GK, Carlson TA (1973) Core electron binding energies in some Group IIIA, VB, and VIB compounds. Inorg Chem 12:2450–2453

[51] Charton P, Gengembre L, Armand P (2002) TeO_2–WO_3 glasses: Infrared, XPS and XANES structural characterizations. J. Solid State Chem. 168:175–183

[52] Mekki A, Khattak GD, Wenger LE (2009) XPS and magnetic studies of vanadium tellurite glasses. J Electron Spectrosc Relat Phenom 175:21–26

[53] Babu S, Rajput P, Ratnakaram YC (2016) Compositional-dependent properties of Pr^{3+}-doped multicomponent fluorophosphate glasses for visible applications: a photoluminescence study. J Mater Sci 51:8037–8054. doi:10.1007/s10853-016-0073-7

[54] Alhalawani AMF, Towler MR (2016) The effect of $ZnO \leftrightarrow Ta_2O_5$ substitution on the structural and thermal properties of SiO_2–ZnO–SrO–CaO–P_2O_5 glasses. Mater. Charact 114:218–224

[55] Khattak GD, Salim MA (2002) X-ray photoelectron spectroscopic studies of zinc–tellurite glasses. J Electron Spectrosc Relat Phenom 123:47–55

[56] Speranza G, Ferrari M, Bettinelli M (1999) X-ray photoemission study of Pr^{3+} in zinc borate glasses. Philos Mag B 79:2145–2155

[57] Mekki A, Holland D, McConville CF, Salim M (1996) An XPS study of iron sodium silicate glass surfaces. J Non-Cryst Solids 208:267–276

[58] Heo J, Lam D, Sigel GH Jr, Mendoza EA, Hensley DA (1992) Spectroscopic analysis of the structure and properties of alkali tellurite glasses. J Am Ceram Soc 75:277–281

[59] Hoppe U, Yousef E, Russel C, Neuefeind J, Hannon AC (2002) Structure of vanadium tellurite glasses studied by neutron and X-ray diffraction. Solid State Commun. 123:273–278

[60] Sekiya T, Mochida N, Ohtsuka A, Tonokawa M (1992) Raman spectra of $MO_{1/2}$–TeO_2 (M = Li, Na, K, Rb, Cs and Tl) glasses. J Non-Cryst Solids 144:128–144

[61] Tanaka K, Yoko T, Yamada H, Kamiya K (1988) Structure and Ionic Conductivity of $LiCl$–Li_2O–TeO_2 glasses. J Non-Cryst Solids 103:250–256

[62] Chowdari BVR, Kumari PP (1996) Thermal, electrical and XPS studies of $Ag_2O·TeO_2·P2O_5$ glasses. J Non-Cryst Solids 197:31–40

[63] Bachvarova-Nedelcheva A, Iordanova R, Kostov KL, Yordanov St, Ganev V (2012) Structure and properties of a non-traditional glass containing TeO_2, SeO_2 and MoO_3. Opt Mater 34:1781–1787

[64] Salim MA, Khattak GD, Tabet N, Wenger LE (2003) X-ray photoelectron spectroscopy (XPS) studies of copper–sodium tellurite glasses. J Electron Spectrosc Relat Phenom 128:75–83

[65] Mekki A, Khattak GD, Wenger LE (2005) Structural and magnetic properties of MoO_3–TeO_2 glasses. J Non-Cryst Solids 351:2493–2500

[66] Moawad HMM, Jain H, El-Mallawany R, Ramadan T, El-Sharbiny M (2002) Electrical conductivity of silver vanadium tellurite glasses. J Am Ceram Soc 85:2655–2659

[67] Marjanovic S, Toulouse J, Jain H, Sandmann C, Dierolf V, Kortan AR, Kopylov N, Ahrens RG (2003) Characterization of new erbium-doped tellurite glasses and fibers. J Non-Cryst Solids 322:311–318

[68] Pal M, Hirota K, Tsujigami Y, Sakata H (2001) Structural and electrical properties of MoO_3–TeO_2 glasses. J Phys D Appl Phys 34:459–464

[69] Zatsepin DA, Zatsepin AF, Boukhvalov DW, Kurmaev EZ, Pchelkina ZV, Gavrilov NV (2016) Electronic structure and photoluminescence properties of Zn-ion implanted silica glass before and after thermal annealing. J Non-Cryst Solids 432(B):183–188

[70] Medda MP, Piccaluga G, Pinna G, Bettinelli M, Cormier G (1994) Coordination of Eu_{3+} ions in a phosphate glass by X-ray diffraction. Z. Naturforsch 49(a):977–982

[71] Hurt JC, Phillips CJ (1970) Structural role of zinc oxide in glasses in the system Na_2O–ZnO–SiO_2. J Am Ceram Soc 53:269–273

[72] Bashter II (1997) Calculation of radiation attenuation coefficients for shielding concretes. Ann Nucl Energy 24:1389–1401

[73] Singh VP, Badiger NM, Kaewkhao J (2014) Radiation shielding competence of silicate and borate heavy metal oxide glasses: comparative study. J Non-Cryst Solids 404:167–173

[74] Singh VP, Badiger NM (2015) Shielding efficiency of lead borate and nickel borate glasses for gamma rays and neutrons. Glass Phys Chem 41:276–283

[75] Sayyed MI (2016) Investigations of gamma ray and fast neutron shielding properties of tellurite glasses with different oxide compositions. Can J Phys 94:1133–1137